Supporting Information

Sulfur-rich N-doped Co$_9$S$_8$ catalyst for highly efficient and durable overall water electrolysis application

Abu Talha Aqueel Ahmed,[1] | Jonghoon Han[1], | Giho Shin[1], | Sunjung Park[1], | Seungun Yeon[1], | Youngsin Park,[2] | Hyungsang Kim,*[1] | Hyunsik Im*[1]

[1] Division of Physics and Semiconductor Science, Dongguk University, Seoul 04620, South Korea

[2] Department of Chemistry, College of Natural Science, Ulsan National Institute of Science and Technology (UNIST), Ulsan 44919, Korea

Correspondence E–mail: hskim@dongguk.edu, hyunsik7@dongguk.edu
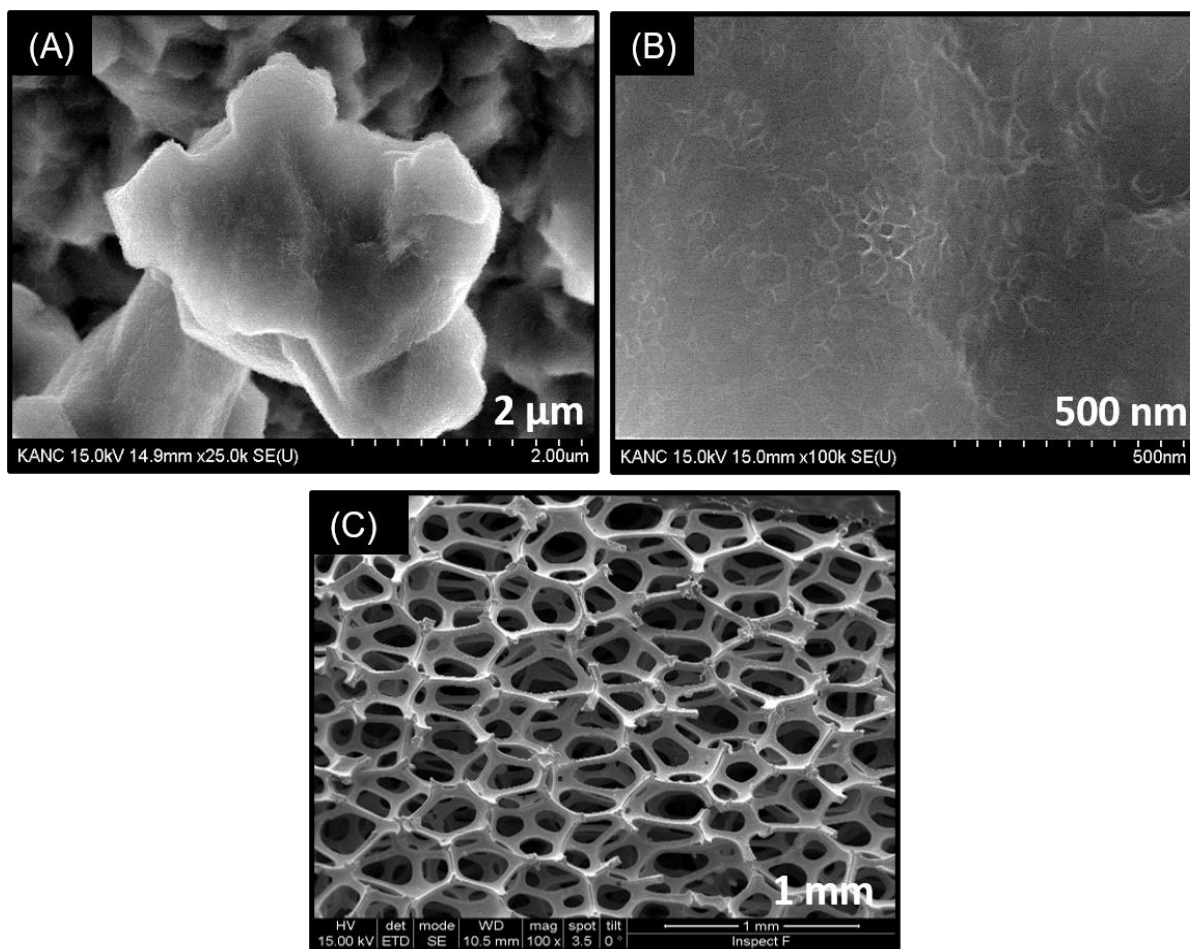
Supplementary Results

FIGURE S1. FE-SEM images of the N-Co$_9$S$_8$ catalyst electrode recorded at (A) low and (B) high magnifications. (C) FE-SEM image of the bare NF substrate recorded at low magnification demonstrating the three-dimensional porous architecture.
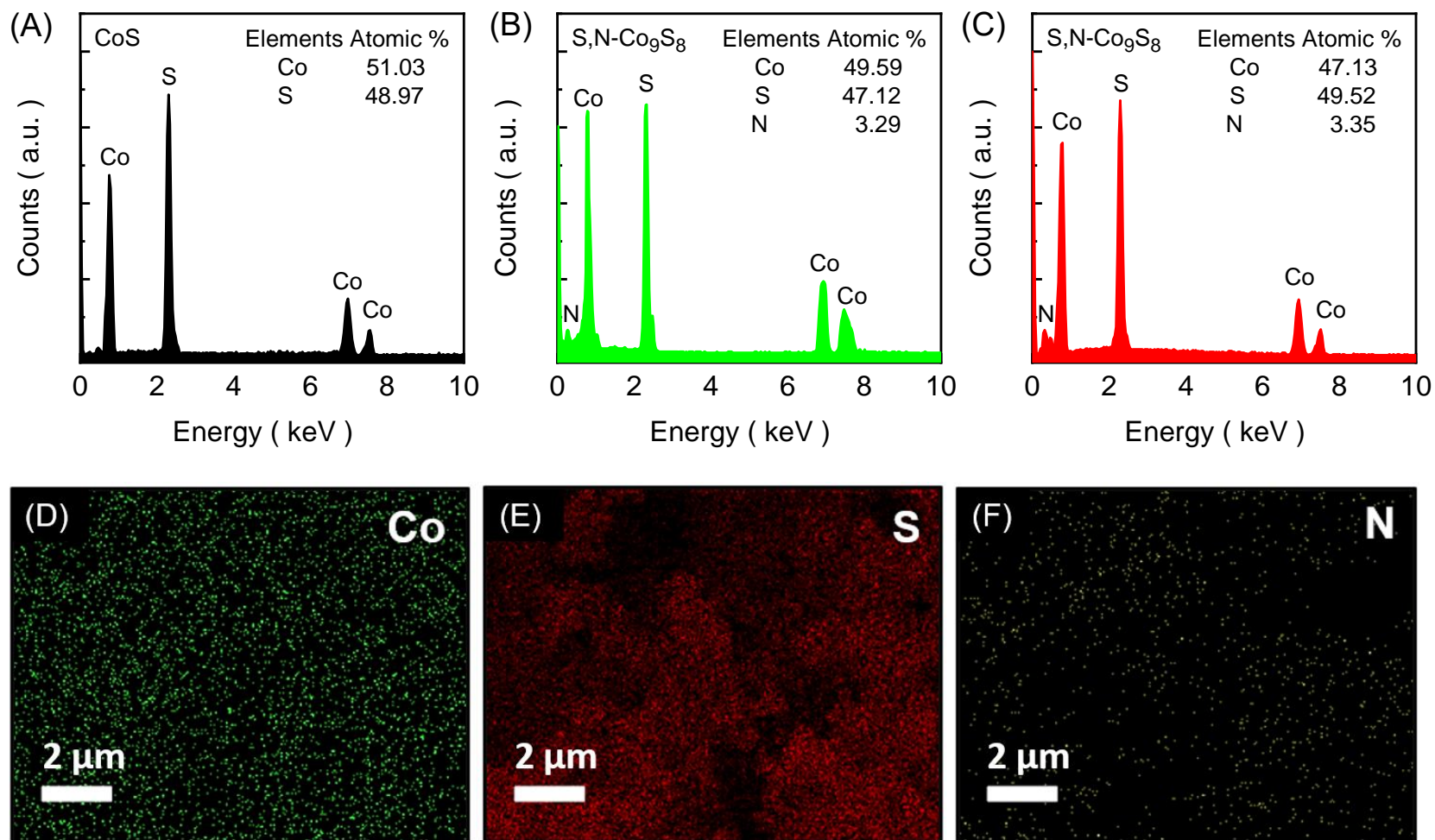
FIGURE S2. EDS spectra of the (A) CoS, (B) N-Co_9S_8, and (C) S,N-Co_9S_8 catalyst electrodes. EDS image mapping of the S,N-Co_9S_8 catalyst electrode, showing uniform distributions of the constituent (D) Co, (E) S, and (F) N elements.
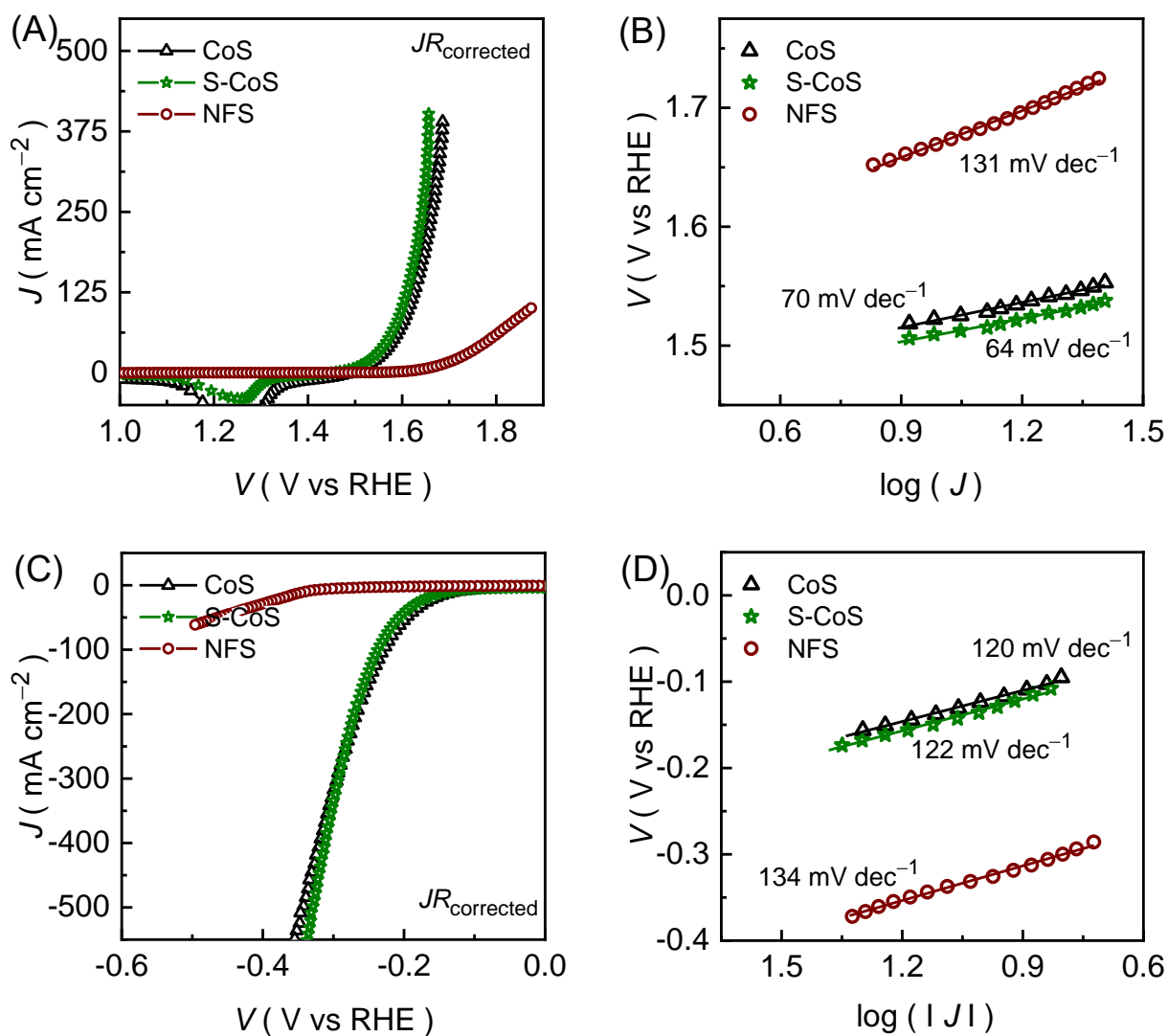
FIGURE S3. (A) OER polarization curves, (B) associated Tafel plots, (C) HER polarization curves, and (D) associated Tafel plots for the bare NF substrate (NFS), as-obtained CoS, and anion-exchange CoS (S-CoS) catalysts.
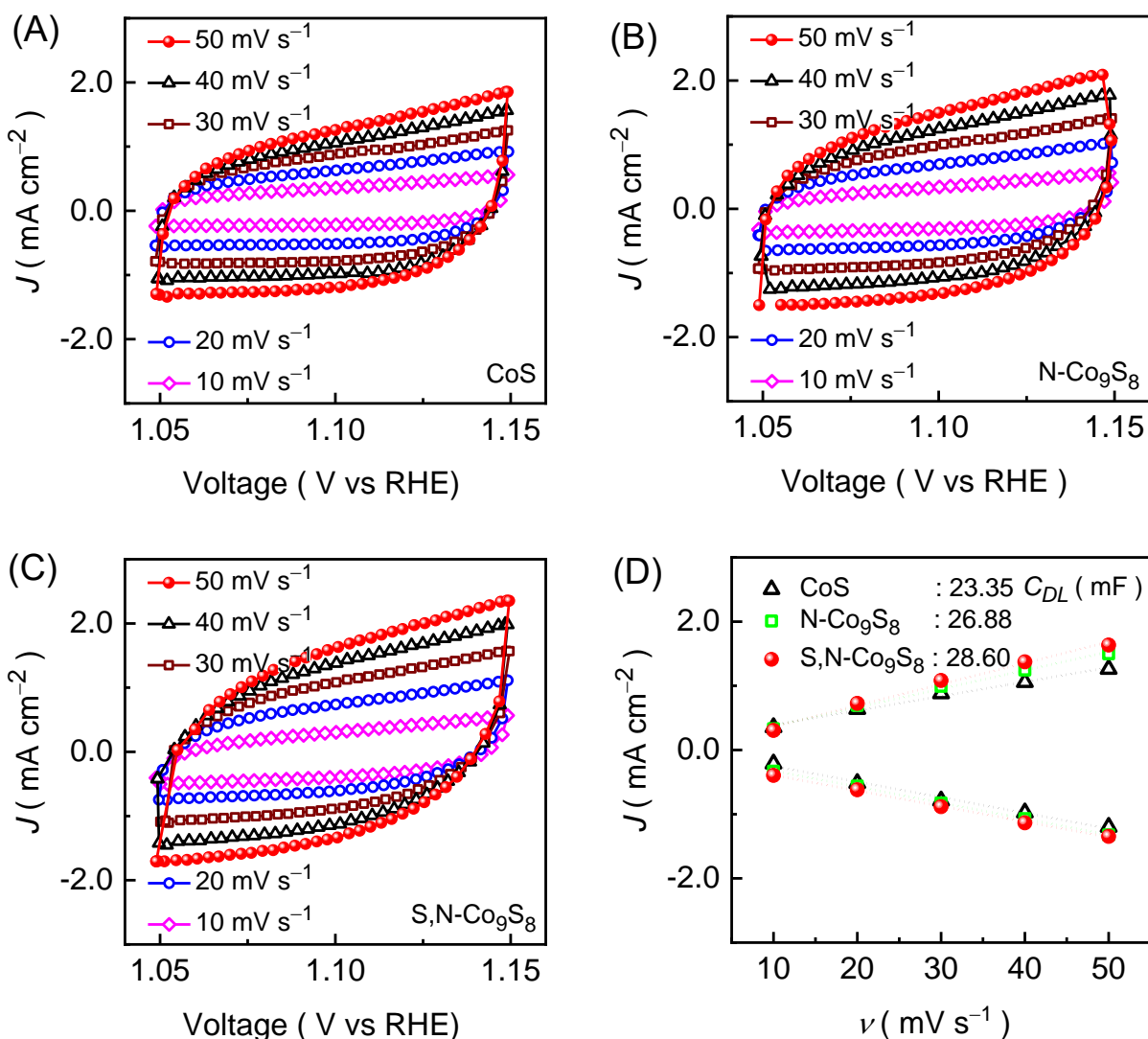
FIGURE S4. CV curves for the (A) CoS, (B) N-Co₉S₈, and (C) S,N-Co₉S₈ catalysts at various current rates in the linear charging region. (D) Non–Faradaic current density obtained from the CV curves at 1.10 V (*vs*. RHE) as a function of the scan rate. Notably, the values of C_{DL} obtained from the anodic and cathodic current were averaged and are presented in the Figure S4D.
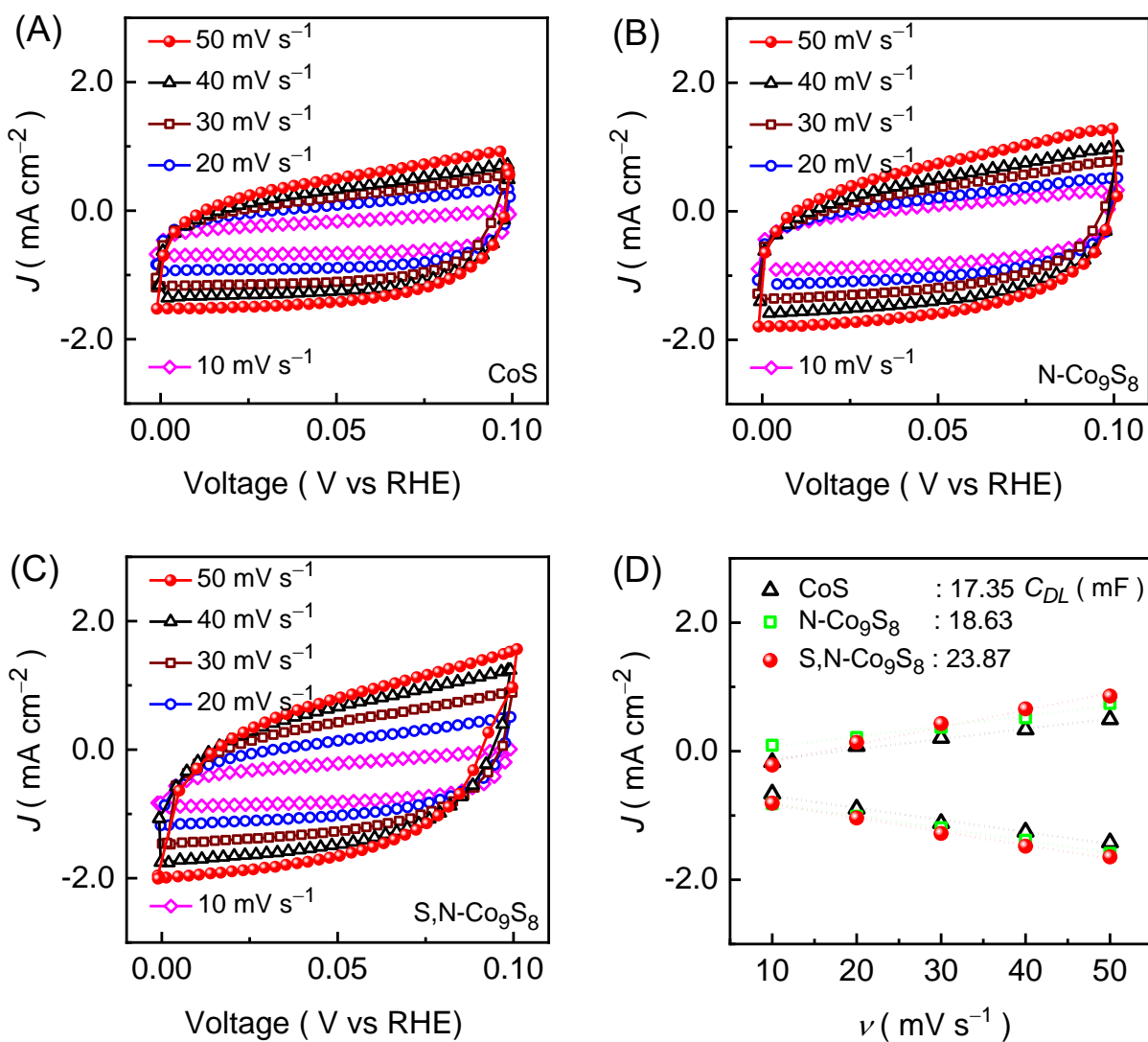
FIGURE S5. Non–Faradaic CV curves for the (A) CoS, (B) N-Co₉S₈, and (C) S,N-Co₉S₈ catalyst electrodes at various current rates. (D) Obtained current density CoS, N-Co₉S₈, and S,N-Co₉S₈ catalysts in the linear charging region at 0.05 V (*vs*. RHE) as a function of scan rate. Notably, the average values of C_{DL} is presented in the Figure S5D.

The accessible electrochemically active surface area (*ECSA*) associated with double-layer capacitance (C_{DL}) in the non-Faradaic CV curve region was measured between 1.05 and 1.15 V (*vs*. RHE) for the OER active sites at various scan rates (10, 20, 30, 40, and 50 mV s^{-1}). The similar CV curves were also recorded between 0.00 and 0.10 V (*vs*. RHE) for the OER active sites. Figures S4A-C,S5A-C show the obtained non-Faradaic CV curves for the CoS, N-Co$_9$S$_8$, and S,N-Co$_9$S$_8$ catalyst. Both the anodic and cathodic current densities (J_{DL}) were supposed to be entirely because of non-Faradaic capacitance current contribution.[S1] Figures S4D,S5D show the "*J_{DL} vs. v*" plots for the CoS, N-Co$_9$S$_8$, and S,N-Co$_9$S$_8$ catalysts, with the double-layer current density obtained at 1.10 and 0.05 V (*vs*. RHE) under various scan rates. The C_{DL} and *ECSA* are determined based on Figures S4,S5 and Eqs. (1) and (2). The S,N-Co$_9$S$_8$ catalyst exhibits a significantly higher *ECSA* of 715 and 597 cm^{-2} for the OER and HER, respectively, than the CoS (584 and 434 cm^{-2}) and N-Co$_9$S$_8$ (672 and 466 cm^{-2}) catalysts. The enhanced *ECSA* of the S,N-Co$_9$S$_8$ catalyst could be a result of the change in the electronic structure associated with the interaction between the heteroatoms and the host material, which might have affected the surface chemistry of the active catalyst, resulting in efficient election/ion transport throughout the 3D polyhedral structure.[38]

Table S1. Comparative electrocatalytic OER activity for the CoS, N-Co$_9$S$_8$, and S,N-Co$_9$S$_8$ catalysts measured in KOH (1.0 M) medium.

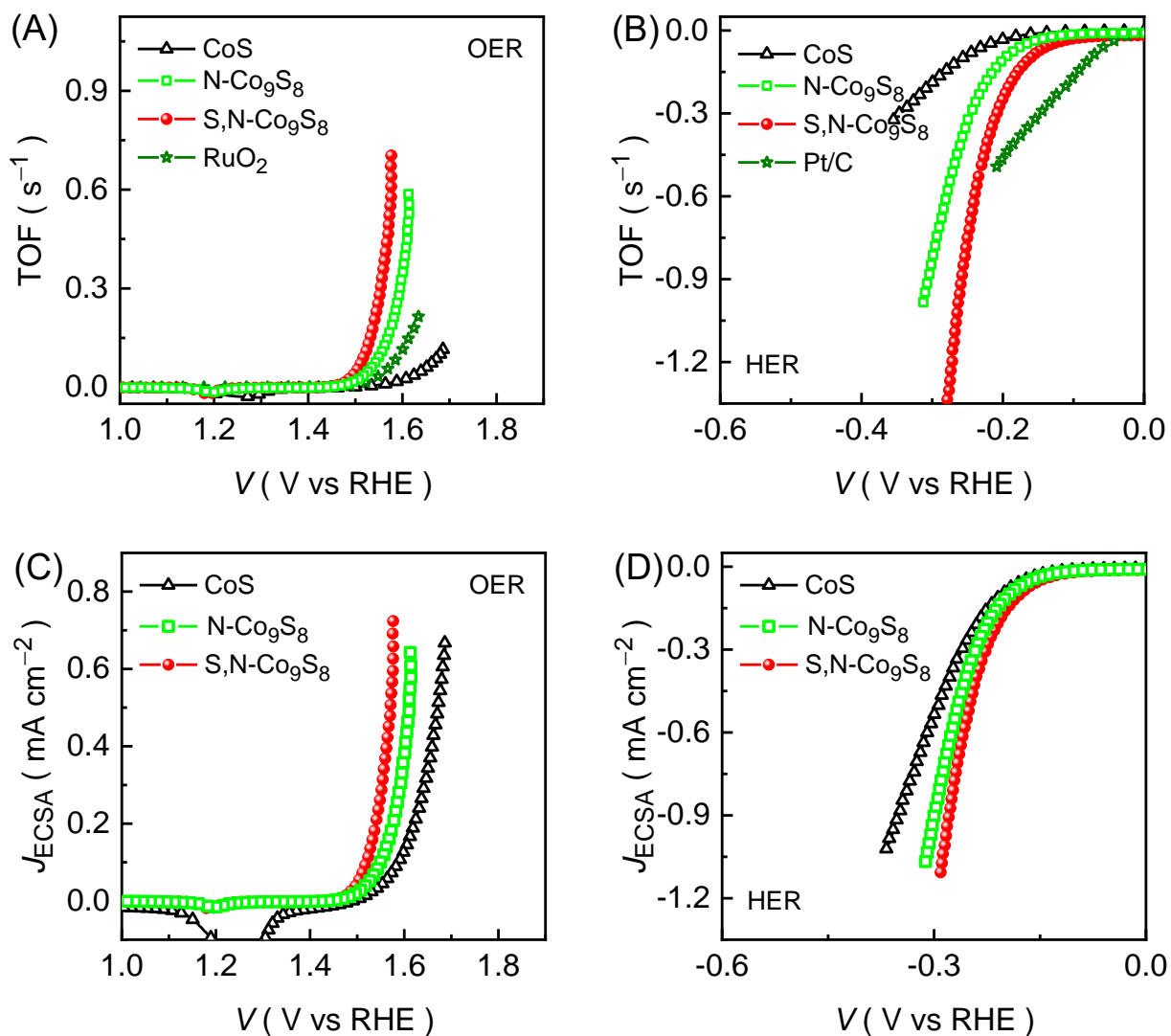| Electrocatalyst	Overpotential (*η*; mV) @*J* (*J* = 10 mA cm^{-2})	Tafel slope (mV dec^{-1})	*ECSA* (cm^2)	TOF@320 mV (s^{-1})
CoS	292	70	584	0.0087
N-Co$_9$S$_8$	259	66	672	0.0933
S,N-Co$_9$S$_8$	244	47	715	0.2625

FIGURE S6. "TOF *vs.* V (RHE)" plot of all of the prepared catalysts for electrocatalytic (A) OER and (B) HER activity. *ECSA*-corrected (A) OER and (D) HER polarization curves measured at 5.0 mV s^{-1} in an alkaline KOH electrolyte (1.0 M).

The turn-over frequency (TOF) for the CoS, N-Co$_9$S$_8$, and S,N-Co$_9$S$_8$ catalysts was calculated using the following equation:[S2,33]

$$TOF = (J_{DL} \times A) / (F \times n \times N) \tag{S1}$$

where F, A, n, and N represents the Faraday constant (96,485.3329 A s mol^{-1}), the loading area, the number of moles for the active catalyst, and number of electrons per mole, respectively. For the electrocatalytic OER process, the value of "N" is 4, while it is 2 for the electrocatalytic HER process because of the four and two electrons per mole of oxygen and hydrogen, respectively. Figure S6A,B show the "TOF *vs.* V" plots for the CoS, N-Co$_9$S$_8$, and S,N-Co$_9$S$_8$ catalysts obtained from Figure 5A,C using Eq. (S1). The estimated TOF at 320 mV for all of the catalysts during the OER process is presented in Table S1. The S,N-Co$_9$S$_8$ catalyst achieves a higher TOF of 0.2625 s^{-1} than those of the CoS (0.0087 s^{-1}) and N-Co$_9$S$_8$ (0.0933 s^{-1}) catalysts. The S,N-Co$_9$S$_8$ catalyst also exhibits a higher TOF of 0.2445 s^{-1} during the HER process at –275 mV (Table S4), and this TOF is further higher than those of the CoS (0.0322 s^{-1}) and N-Co$_9$S$_8$ (0.1067 s^{-1}) catalysts. Thus, results in faster reaction kinetics compared to all other catalysts during the electrocatalytic OER and HER processes. Moreover, the intrinsic reaction kinetics can be further assessed using the *ECSA*-based specific current density. Figure S6C,D show the *ECSA*-based OER and HER polarization curves. Yet again, the S,N-Co$_9$S$_8$ catalyst archives the lowest overpotential for each J_{ECSA} for both the OER and HER processes, confirming its faster intrinsic reaction kinetics among all catalysts.
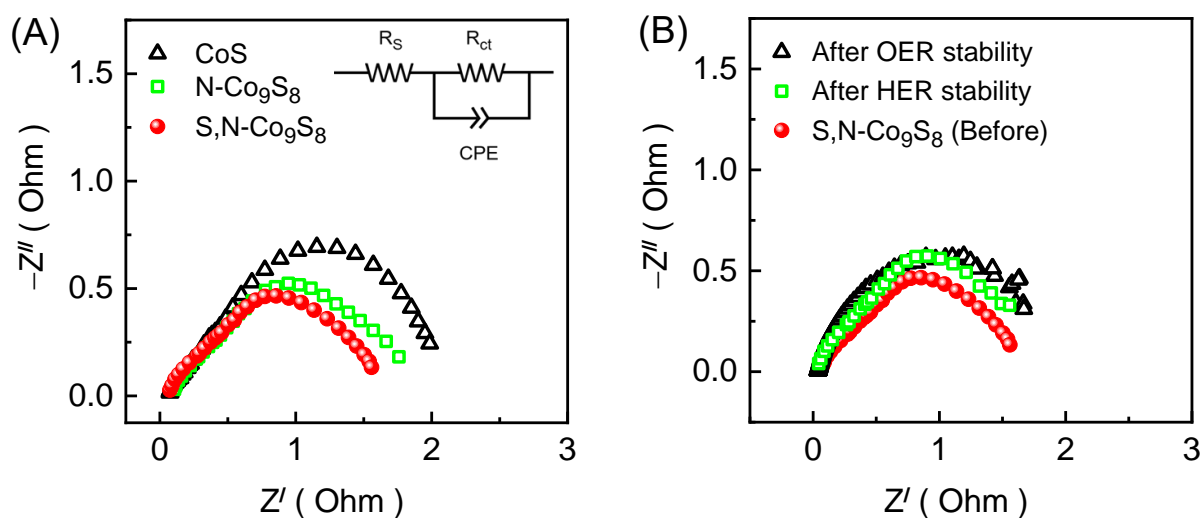
FIGURE S7. (A) EIS curves of the CoS, N-Co$_9$S$_8$, and S,N-Co$_9$S$_8$ catalysts recorded in a frequency range between 0.1 and 10 kHz at a biasing voltage of 0.3 V. (B) EIS curves of the S,N-Co$_9$S$_8$ catalyst measured before and after the long-term (50 h) chronopotentiometric stability test.

The EIS (Nyquist impedance) curves for the CoS, N-Co$_9$S$_8$, and S,N-Co$_9$S$_8$ catalysts were measured at a biasing potential of 0.3 V in a frequency range of 0.1-10 kHz with an applied AC signal amplitude of 10 mV. Figure S7A presents the Nyquist impedance curves for the CoS, N-Co$_9$S$_8$, and S,N-Co$_9$S$_8$ catalysts fitted using Z-view software with the help of a simple tank circuit (inset of Figure S7A). The semicircle component of the Nyquist impedance curve represents the charge transfer resistance (R_{ct}), and its intersection along the Z$'$–axis designates the internal resistance (R_S), which is a combination of the intrinsic resistance of the substrate and electrolyte.[S3,S4] The S,N-Co$_9$S$_8$ catalyst had an R_S and R_{ct} of 0.074 and 1.568 Ω, lower than those of the CoS (0.085 and 2.047 Ω) and S,N-Co$_9$S$_8$ (0.082 and 1.765 Ω) catalysts. The enhanced electron/ion transport is a result of the varied electronic structure of the S,N-Co$_9$S$_8$ catalyst compared with the CoS and N-Co$_9$S$_8$ catalysts, which had an effect on the exposed electrocatalytically active sites for the electrochemical reactions.

Table S2. Comparative electrocatalytic OER performance of our polyhedral S,N-Co$_9$S$_8$ catalyst with previously reported cobalt sulfide based catalyst.

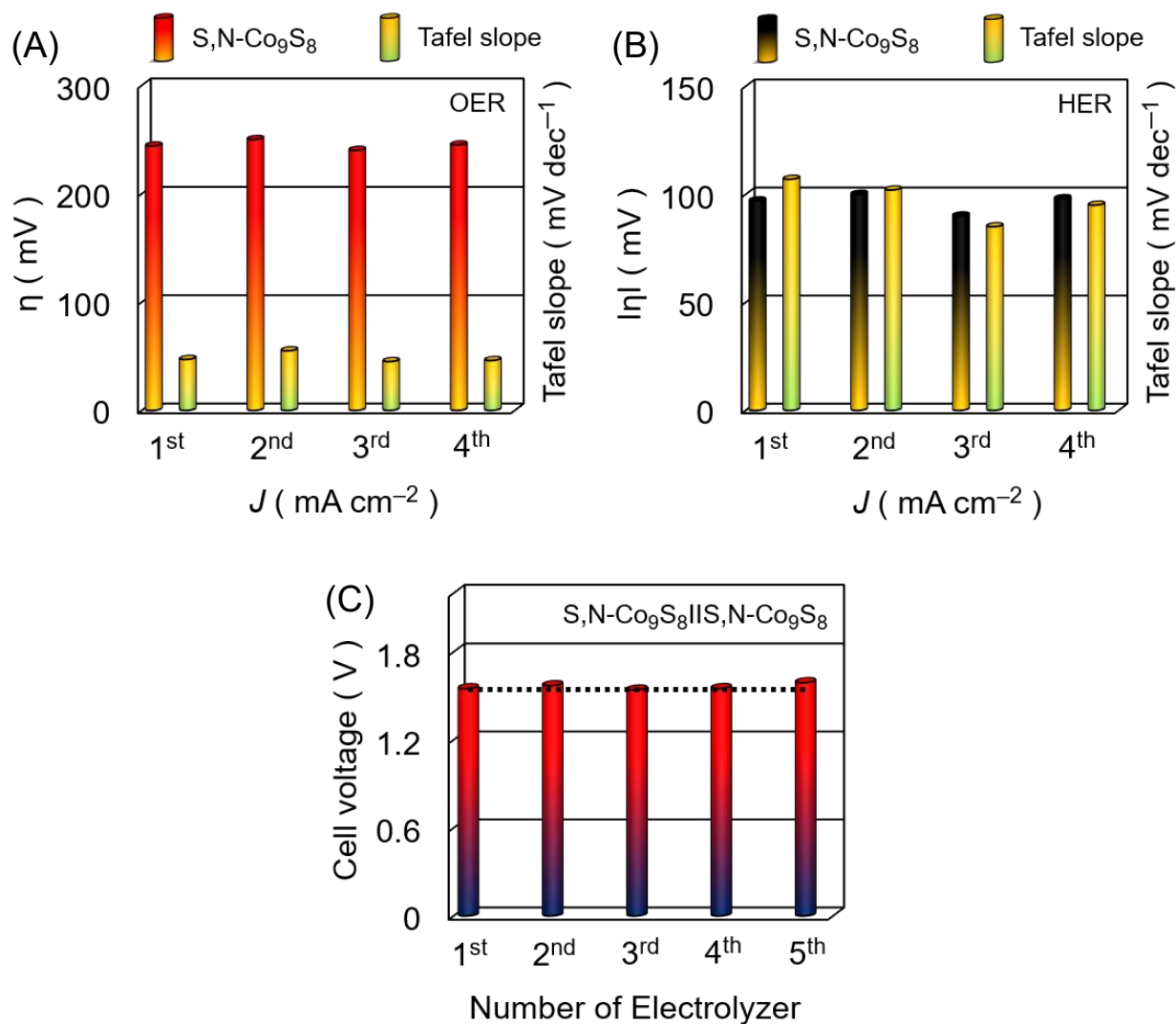| No.	Samples	Overpotential @10 mA cm^{-2}	Tafel slope (mV dec^{-1})	Stability (h)	J (mA cm^{-2})	Ref.
1	MOF driven CoS$_2$	298	94	20	1.53 V	25
2	CoS$_2$	315	96	-	-	26
3	Co$_9$S$_8$ HNSs	342	104	-	-	27
4	Co$_3$S$_4$ HNSs	307	108	-	-	27
5	CoS$_2$ HNSs	290	57	12	10	27
6	Co$_3$S$_4$	287	184	-	-	28
7	Co$_3$S$_4$/AC/-20	270	93	48	10 mV s^{-1}	29
8	Co$_9$S$_8$	315	87	-	-	30
9	Polyhedral S,N-Co$_9$S$_8$	244 279 297	47	50 50 50	10 50 100	Present Work

FIGURE S8. Reliability of the S,N-Co$_9$S$_8$ catalyst for the (A) electrocatalytic OER and (B) HER activities in an alkaline 1.0 M KOH electrolyte medium. (C) Reliability of the bifunctional S,N-Co$_9$S$_8$||S,N-Co$_9$S$_8$ catalyst obtained from the series of the electrolyzer test under similar experimental conditions.
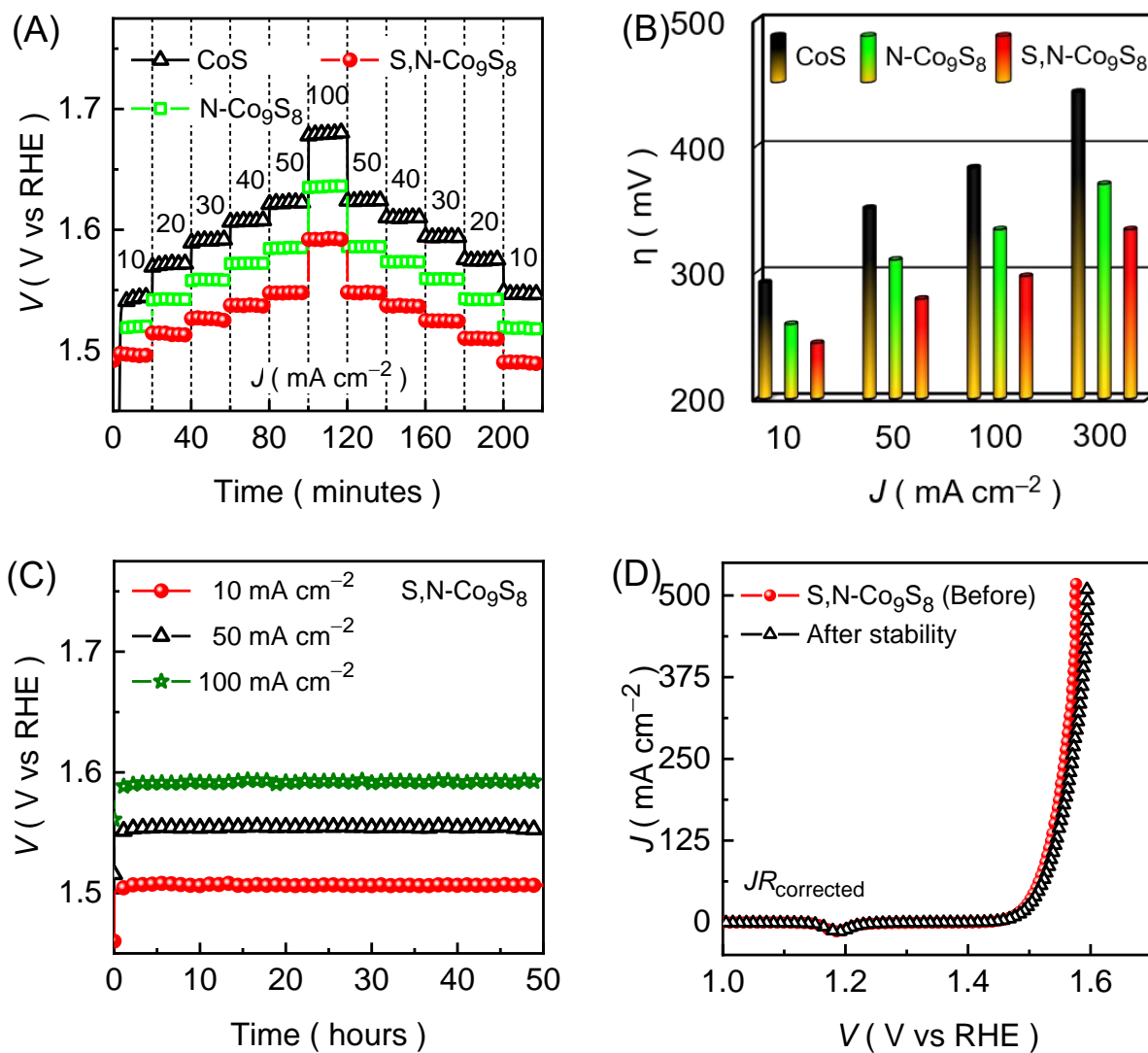
FIGURE S9. (A) Chronopotentiometric voltage-step profile as a function of the current density rate and the (B) obtained overpotential for the CoS, N-Co$_9$S$_8$, and S,N-Co$_9$S$_8$ catalysts at various current densities. (C) Chronopotentiometric electrolysis curves of the S,N-Co$_9$S$_8$ catalyst at low and high current densities and (D) polarization curves before and after the long-term stability for the S,N-Co$_9$S$_8$ catalyst.
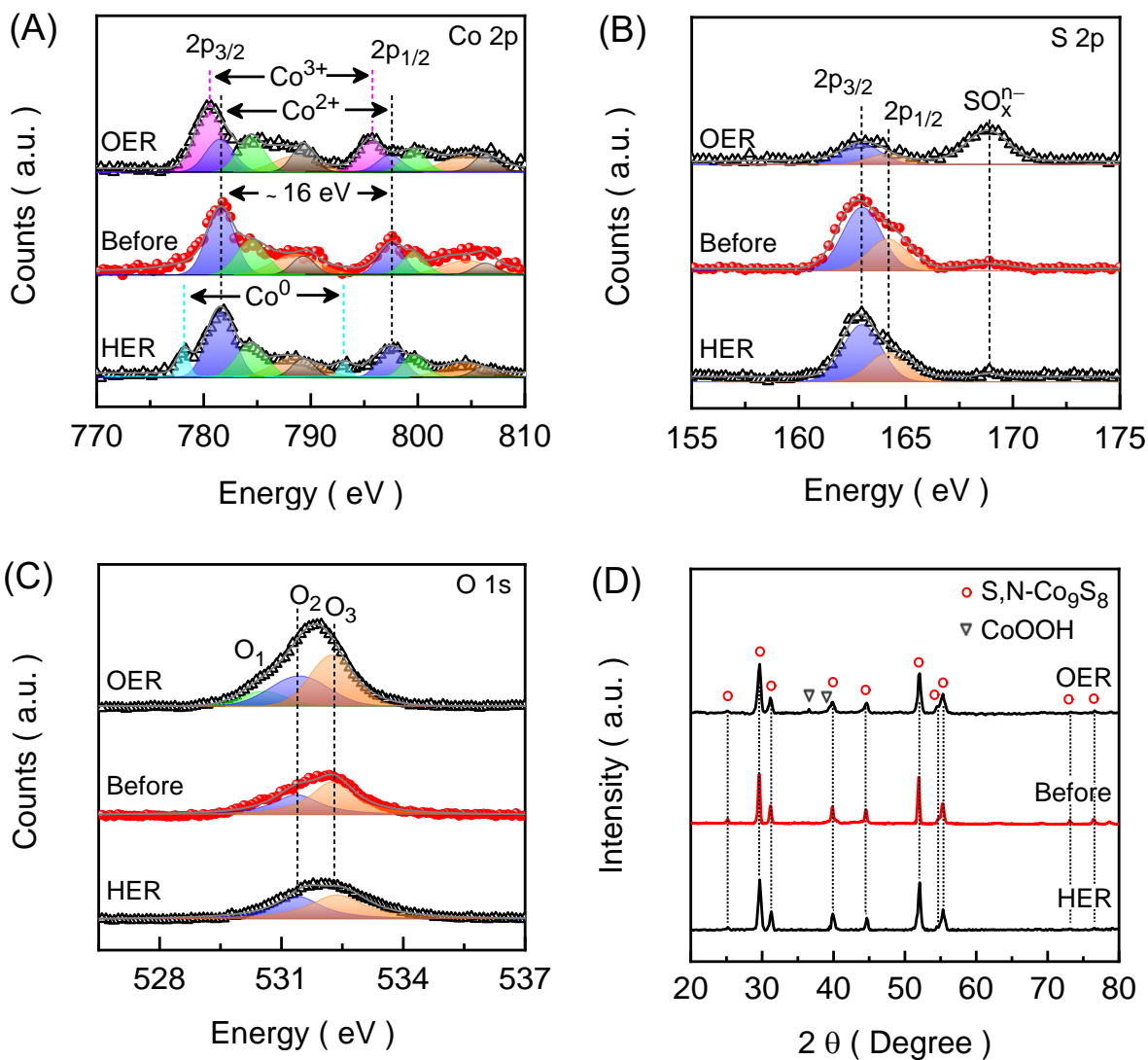
FIGURE S10. High-resolution XPS spectra after post-stability measurements. (A) Co 2p, (B) S 2p, and (C) O 1s emission spectra for the S,N-Co$_9$S$_8$ catalyst. (D) Post-stability XRD spectra for the S,N-Co$_9$S$_8$ catalyst.

Figure S10 shows the high-resolution Co 2p and S 2p XPS spectra for the S,N-Co_9S_8 catalyst measured after the long-term chronopotentiometric OER and HER stabilities. An insignificant change in the intensities is observed for the Co 2p peaks after the electrocatalytic OER stability. However, the spin-energy separation changes from 16.00 to 15.18 eV (Figure S10A). The change in the spin-energy separation is a result of fractional transformation of Co^{2+} into Co^{3+} state, confirming the formation of CoOOH species upon the electrooxidation process.[S5,26] Besides, an abrupt change in the S 2p peak intensity is observed (Figure S10B), suggesting the loss of sulfur atoms, whereas the additional wide-ranging peak formed after the OER stability. This broad peak is related to SO_x^{n-} originated because of the surface oxidation during the electrooxidation process in alkaline KOH medium.[26] The formation of the CoOOH phase leads to an increase in the oxygen content, illustrated by the stronger O 1s emission peak intensity (Figure S10C).[S3] This O 1s peak can be deconvoluted into three main peaks, O_1 (530.56 eV), O_2 (531.44 eV), and O_3 (532.27 eV), which are associated with metal-oxygen bonds, nonstoichiometric oxygen coordination, and the multiplicity of physiosorbed/chemisorbed water near or on the surface, respectively.[6] On the other hand, the Co and S peak intensities and positions are remains same after the electrocatalytic HER stability, whereas an additional doublet formed with a spin-energy separation of ~ 15 eV related to Co^0 state, which is usually occur after the HER activity.[33]
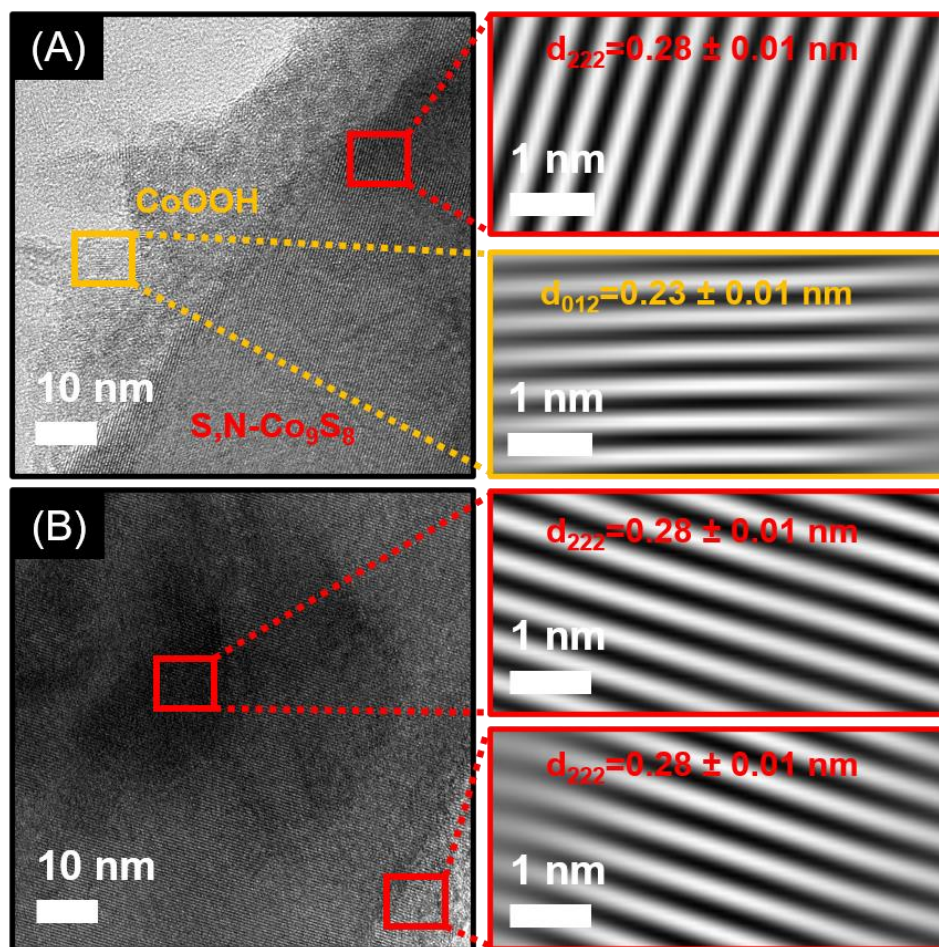
FIGURE S11. HR-TEM images of the S,N-Co$_9$S$_8$ catalyst measured after the (A) OER and (B) HER stabilities in a 1.0 M KOH electrolyte. The HR-TEM images reveal that the partial *in–situ* phase transformation of the active catalyst phase into CoOOH (JCPDS card no. 07-0169; Figure S11A) occurred during the OER stability test might be due to an electrooxidation, while the S,N-Co$_9$S$_8$ phase is intact after the HER stability test (Figure S11B).
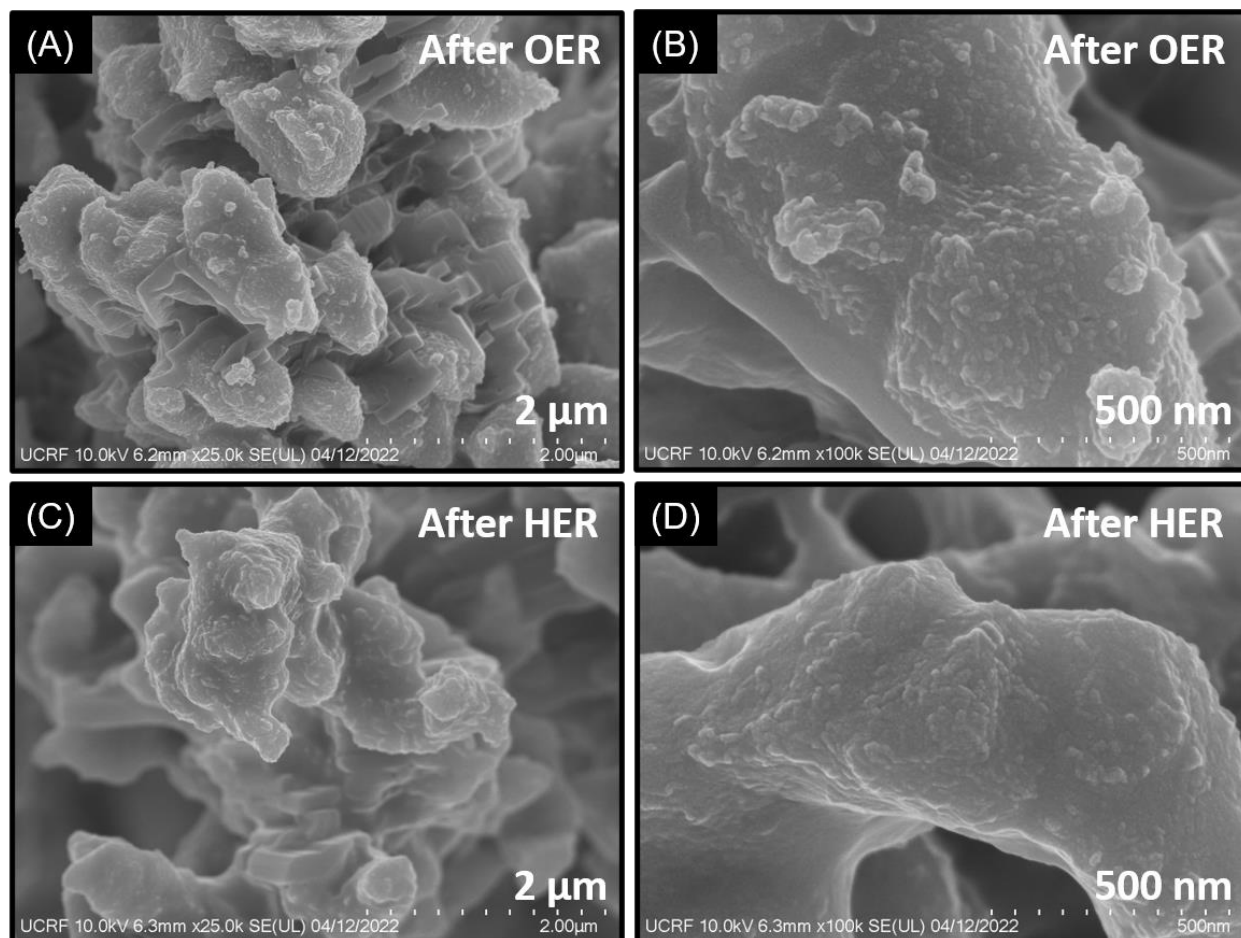
FIGURE S12. FE-SEM images of the S,N-Co$_9$S$_8$ catalyst measured at low and high magnifications after the (A,B) OER and (C,D) HER stabilities in an alkaline KOH (1.0 M) electrolyte medium.

Table S3. Comparative electrocatalytic HER performance of our polyhedral S,N-Co_9S_8 catalyst with previously reported cobalt sulfide based catalyst.

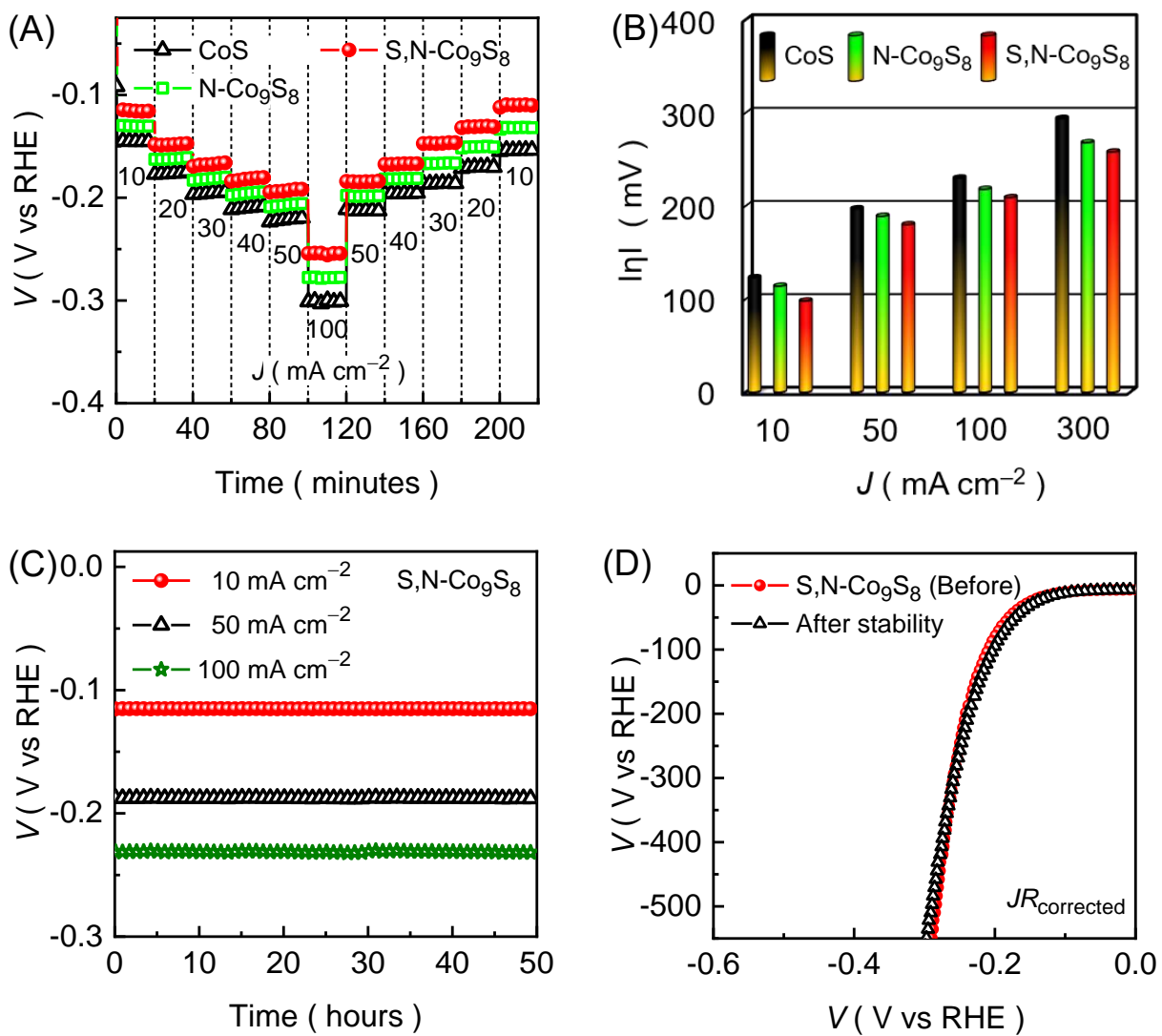| No.	Samples	Overpotential @10 mA cm^{-2}	Tafel slope (mV dec^{-1})	Stability (h)	J (mA cm^{-2})	Ref.
1	MOF driven CoS_2	196	113	20	– 0.2 V	25
2	CoS_2	249	228	-	-	31
3	Co_9S_8 HNSs	267	139	-	-	27
4	Co_3S_4 HNSs	221	111	-	-	27
5	CoS_2 HNSs	193	100	12	10	27
6	Co_3S_4	266	132.2	-	-	28
7	Co_3S_4 NS	93	228	-	-	32
8	Co_9S_8	331	55.1	-	-	30
9	Polyhedral S,N-Co_9S_8	98 180 209	107	50 50 50	10 50 100	**Present Work**

FIGURE S13. (A) Chronopotentiometric potential response at various current densities and the (B) attained overpotential for the CoS, N-Co$_9$S$_8$, and S,N-Co$_9$S$_8$ catalysts at different current densities. (C) Chronopotentiometric stability curves at low and high current densities and the (D) obtained polarization curves measured before and after the long-term stability for the S,N-Co$_9$S$_8$ catalyst.

Table S4. Comparative electrocatalytic HER activities for the CoS, N-Co_9S_8, and S,N-Co_9S_8 catalysts recorded in 1.0 M KOH electrolyte.

Electrocatalyst	Overpotential (η; mV) @J (J = 10 mA cm^{-2})	Tafel slope (mV dec^{-1})	*ECSA* (cm^2)	TOF@-275 mV (s^{-1})
CoS	-123	120	~ 434	0.0322
N-Co_9S_8	-114	118	~ 466	0.1067
S,N-Co_9S_8	-92	107	~ 597	0.2445

SUPPORTING REFERENCES

S1. Ahmed ATA, Bathula C, Soni R, Kim HS, Im H, Lee SW, Kim WK, Gedi S, Kadam AN. Nanostructurally engineered TiO_2 embedded Mentha aquatica biowaste derived carbon for supercapacitor applications. *Chemosphere.* 2022;289:133197.

S2. Seo B, Jung GY, Sa YJ, Jeong HY, Cheon JY, Lee JH, Kim HY, Kim JC, Shin HS, Kwak SK, Joo SH. Monolayer-Precision Synthesis of Molybdenum Sulfide Nanoparticles and Their Nanoscale Size Effects in the Hydrogen Evolution Reaction. *ACS Nano.* 2015;9:3728-3739.

S3. Ahmed ATA, Hou B, Inamdar AI, Cha S, Kim H, Im H. Morphology Engineering of Self-Assembled Nanostructured $CuCo_2O_4$ Anodes for Lithium-Ion Batteries. *Energy Technol.* 2019;7:1900295.

S4. Ahmed ATA, Soni R, Ansari AS, Lee CY, Kim HS, Im H, Bathula C. Biowaste-derived graphitic carbon interfaced TiO_2 as anode for Lithium-ion battery. *Surface and Interfaces.* 2022;34:102404.

S5. Li P, Zhuang Z, Du C, Xiang D, Zheng F, Zhang Z, Fang Z, Guo J, Zhu S, Chen W. Insights into the Mo-Doping Effect on the Electrocatalytic Performance of Hierarchical Co_xMo_yS Nanosheet Arrays for Hydrogen Generation and Urea Oxidation. ACS Appl Mater Interfaces. 2020;12:40194-40203.